







## Electrostatic extension of magnetic proximity effect in $\text{La}_{0.7}\text{Sr}_{0.3}\text{MnO}_3$

Qianqian Lan <sup>1,\*</sup>, Michael Schnedler <sup>1</sup>, Lars Freter,<sup>1</sup> Chuanshou Wang <sup>2</sup>,  
Kurt Fischer <sup>3</sup>, Philipp Ebert <sup>1</sup> and Rafal E. Dunin-Borkowski <sup>1</sup>

<sup>1</sup>*Ernst Ruska-Centre for Microscopy and Spectroscopy with Electrons (ER-C-1) and Peter Grünberg Institute (PGI-5),  
Forschungszentrum Jülich GmbH, 52425 Jülich, Germany*

<sup>2</sup>*Department of Physics, Southern University of Science and Technology, Shenzhen 518055, People's Republic of China*

<sup>3</sup>*Department of Mechanical and Electrical Engineering, National Institute of Technology,  
Tokuyama College, Gakuendai, Shunan, Yamaguchi 745-8585, Japan*



(Received 19 September 2022; revised 27 June 2023; accepted 25 October 2023; published 28 November 2023)

Magnetic proximity effects are typically limited to a few nanometers due to the short-range nature of the underlying magnetic interactions. Here, we use off-axis electron holography to reveal an electrostatically induced long-range magnetic proximity effect that extends over a distance of 40 nm at a ferromagnetic/paramagnetic interface in  $\text{La}_{0.7}\text{Sr}_{0.3}\text{MnO}_3$ . We show that this behavior results from carrier diffusion and drift across the interface, which changes the  $\text{Mn}^{3+}/\text{Mn}^{4+}$  ratio and hence the local Curie temperature and density of magnetic moments.

DOI: [10.1103/PhysRevB.108.L180410](https://doi.org/10.1103/PhysRevB.108.L180410)

Many fascinating magnetic effects emerge at interfaces between layers with different magnetic orders [1–5]. Interface confinement is intimately related to the magnetic proximity effect, which typically has a spatial extent of only a few atomic layers [3,6–9]. This short extent is due to the underlying physical coupling mechanisms, such as the exchange interaction, the Dzyaloshinsky-Moriya interaction [10], interface states [11–13], rehybridization [14,15], and reconstruction [16], all of which are highly localized. Here, we report an exceptionally long-range magnetic proximity effect reaching  $\sim 40$  nm at a ferromagnetic (FM)/paramagnetic (PM) interface in  $\text{La}_{0.7}\text{Sr}_{0.3}\text{MnO}_3$  (LSMO). This wide extent arises from carrier diffusion and drift across the interface, which changes the  $\text{Mn}^{3+}/\text{Mn}^{4+}$  ratio and thereby the density of magnetic moments and local Curie temperature. We determine the carrier concentration dependence of the Curie temperature and unravel the physical mechanism of the electrostatic extension of magnetic proximity effects, fundamentally reshaping our understanding of micromagnetism in perovskites.

The LSMO film studied here was grown on a 0.5 wt % Nb-doped  $\text{SrTiO}_3$  (001) substrate using pulsed laser deposition, as described in the Supplemental Material [17]. An interruption occurred during growth of the LSMO film, resulting in a decrease in Mn composition. This changes the  $\text{Mn}^{3+}/\text{Mn}^{4+}$  ion ratio, responsible for a decrease in Curie temperature ( $T_C$ ) from approximately  $T_{C1} = 339_{-2}^{+1}$  K to  $T_{C2} = 279 \pm 3$  K between the different sublayers in the film, as measured using superconducting quantum interference device (SQUID) magnetometry in a bath cryostat (for details, see [18]). Between the two  $T_C$  values, the LSMO film therefore exhibits a *spatial* FM to PM transition. It should be noted that this system

exhibits a strain-free, unreconstructed model interface within the same material [18]. Thus, lattice-strain-induced magnetostrictive effects [19] are absent and only  $T_C$  varies between adjacent sublayers as a result of doping. Based on classical micromagnetics, only the exchange interaction is relevant and the extent of the magnetic proximity effect can be expected to be in the 1–3 nm range, which is far below the value measured below.

Figures 1(b) and 1(d) show magnetic induction maps reconstructed from magnetic phase images recorded using off-axis electron holography (EH) at 295 and 280 K, respectively (see Supplemental Material [17]), from the junction between the FM and PM LSMO layers. The density and direction of the phase contours reveal the strength and direction of the projected in-plane magnetic induction. Electron holographic tomography experiments show that no measurable out-of-plane component is present (see Figs. S2–S4 in the Supplemental Material [17]).

The position of the FM/PM LSMO interface was determined by measuring the Mn concentration of the same region in the same lamella using energy-dispersive x-ray (EDX) spectroscopy [Fig. 1(e)]. The results show that the Mn concentration decreases from the FM layer to the PM layer by  $2.7 \pm 0.3\%$  over a distance that has a full width at half maximum of  $6.9 \pm 1.3$  nm, as derived from a hyperbolic tangent fit (red line). The FM/PM interface is defined as the inflection point of the fit (marked by a dashed orange line).

In Figs. 1(b) and 1(d), the gray scale maps show electron optical phase contours that run parallel to the interface on the FM (left) side. The green arrows in Figs. 1(a) and 1(c) visualize the corresponding two-dimensional projected in-plane magnetization (see below for estimate of stray field), derived using a model-based iterative reconstruction algorithm [20], revealing the direction and strength of magnetic moments oriented parallel to the interface. Deep on

\*q.lan@fz-juelich.de

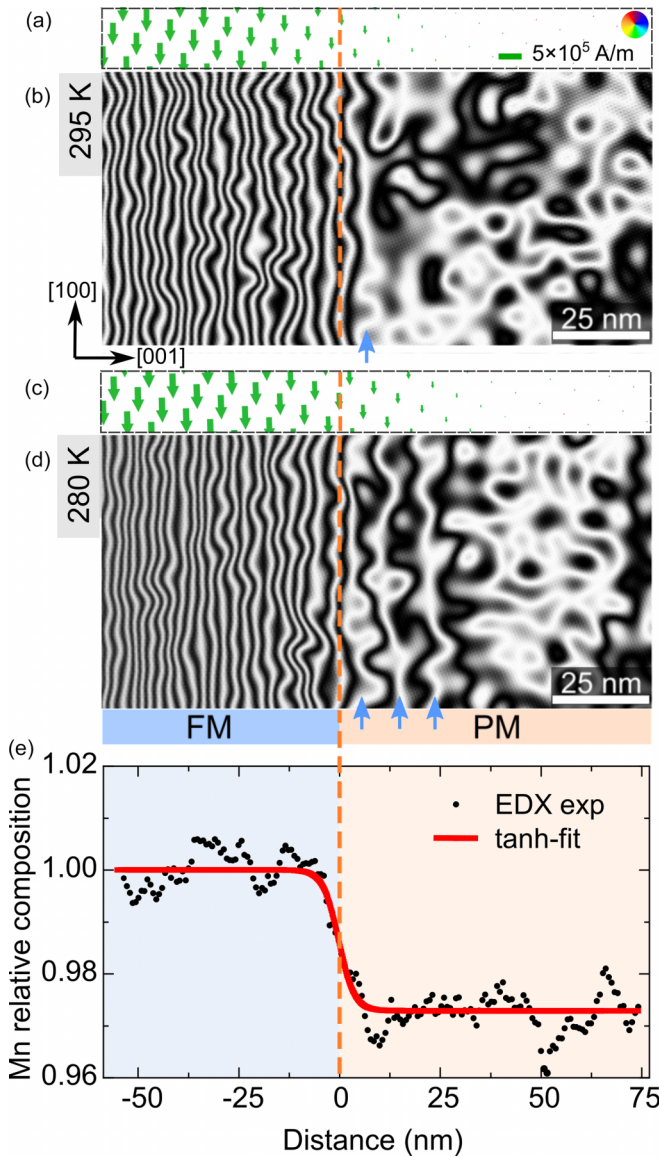


FIG. 1. Magnetic induction maps of a FM/PM interface between two LSMO layers with slightly different Mn compositions (b), (d) determined from the magnetic contribution to the phase shift measured using off-axis electron holography at 295 K and 280 K, respectively. The contour spacing is  $\pi/25$  radians. (a) and (c) show the corresponding magnitude and orientation determined from (b) and (d) using a model-based iterative reconstruction algorithm. (e) Line profile of the Mn composition measured using EDX spectroscopy at the same location as (b) and (d). The inflection point of the hyperbolic tangent fit (red line) is defined as the spatial position of the interface between the FM and PM layers and is marked by a dashed orange line. The noise on the right side (appearing as a circular pattern) in the magnetic induction maps in (b) and (d) is indicative of a PM state, while the vertical lines on the left side result from alignment of the magnetization in the FM layer. The blue arrows mark phase contour lines with weaker alignment of the magnetization penetrating into the PM layer.

the PM (right) side only noise can be discerned, indicating no overall alignment of the magnetic moments, i.e., a PM state. Close to the interface, the phase contour lines increasingly develop a preferential orientation parallel to the interface,

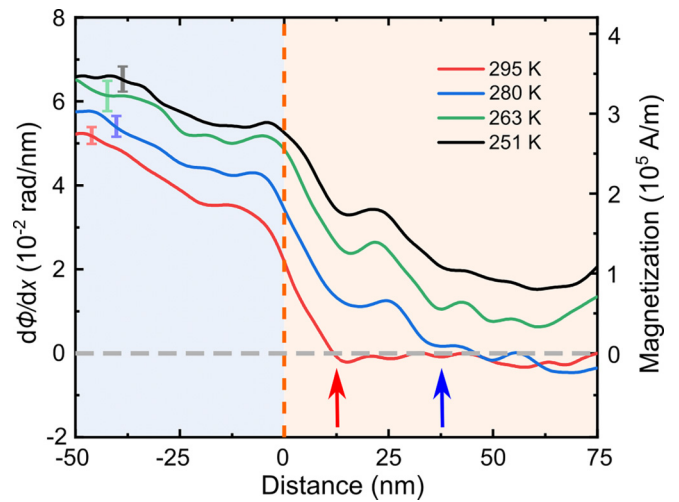


FIG. 2. First derivative of the magnetic contribution to the phase shift  $d\phi/dx$  (left axis) plotted as a function of distance from the PM/FM interface ( $x = 0$  nm) along [001] in the LSMO film at 295 K (red), 280 K (blue), 263 K (green), and 251 K (black). The derivative of the magnetic contribution to the phase shift  $d\phi/dx$  measured using off-axis electron holography can be converted to units of average in-plane magnetization (right axis; see text for details). The slight slope in the FM layer is attributed partially to a small thickness change of the transmission electron microscopy lamella (see Fig. S1 in the Supplemental Material [17]).

indicating a penetration of FM order into the PM layer. This penetration depth increases at lower temperature from  $\sim 10$  nm at 295 K to  $\sim 35$  nm at 280 K.

In order to obtain quantitative insight into the penetration of FM order into the PM layer at the FM/PM interface, Fig. 2 shows the first derivative of the magnetic phase shift  $d\phi/dx$  plotted as a function of position for different temperatures between and below the two  $T_C$  values. Since magnetic fringing fields are negligible according to a MuMax3 simulation (see below), the gradient of the phase shift  $d\phi/dx$  measured using EH is proportional to the average projected in-plane magnetization multiplied by the experimentally determined magnetically active thickness of the lamella in the electron beam direction (see Supplemental Material [17]), with a proportionality constant of  $\frac{2\pi\mu_0 e}{h}$  [21]. The corresponding magnetization values are given on the right axis in Fig. 2. The results show that the magnetization in the FM layer is above  $10^5$  A/m at each investigated temperature. In the PM layer, no magnetization can be detected at 295 and 280 K far (i.e.,  $>40$  nm) from the interface position at both temperatures above  $T_{C2}$ . Close to the interface, a region with nonzero magnetization is present on the PM layer side, with an extent that increases from  $13.3 \pm 1.8$  nm at 295 K to  $38^{+8}_{-4}$  nm at 280 K, revealing that FM order penetrates into the PM layer. At temperatures below  $T_{C2}$ , nonzero magnetization is present everywhere, as the PM layer becomes fully FM.

Since the magnetic properties in this material are governed by the  $\text{Mn}^{3+}/\text{Mn}^{4+}$  double exchange interaction and hence can be influenced by the free-carrier distribution [18], the local variation in electronic properties across the FM/PM interface needs to be considered. For this purpose, changes in the Mn  $L$  edge across the sample were measured us-

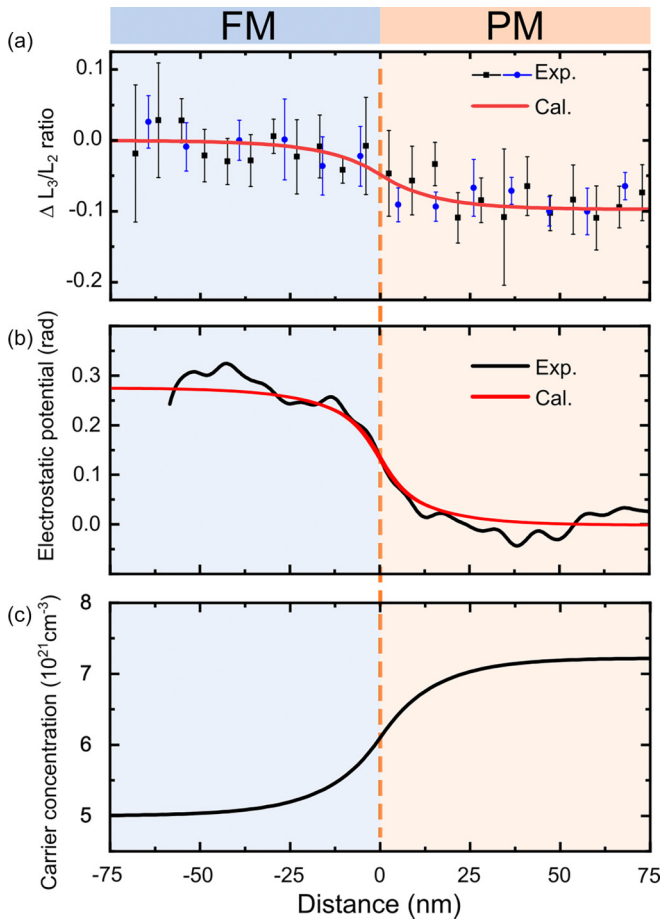


FIG. 3. (a) Change in  $L_3/L_2$ -edge ratio measured using EELS at the same location as in Fig. 1 (black squares) and, for comparison, in a different lamella (blue dots). The red line shows the change in  $L_3/L_2$ -ratio calculated on the basis of carrier diffusion and drift visible in (c). (b) Electrostatic contribution to the phase shift (black) measured using off-axis electron holography at 295 K, compared to a simulation (red) based on the calculated electrostatic potential induced by carrier redistribution [see (c)] and to the change in mean inner potential associated with the change in Mn composition. (c) Carrier concentration plotted as a function of distance from the FM/PM interface.

ing electron-energy-loss spectroscopy (EELS) at 295 K. The resulting integrated  $L_3/L_2$ -edge ratio change is shown in Fig. 3(a). A clear decrease is visible from the FM to the PM layer by  $0.097 \pm 0.015$ . This result indicates a corresponding Mn valence change, which can be quantified using the known linear dependence of the  $L_3/L_2$ -edge ratio on valence state, which has a slope of  $-0.73 \pm 0.11$  [22]. Based on this relationship, we infer a change in Mn valence of  $\Delta V = 0.133 \pm 0.029$  between the FM and PM layer, with a smooth transition between the layers over a width of  $57 \pm 16$  nm at 295 K. This change in valence agrees well with that probed at 150 K below both  $T_{C1}$  and  $T_{C2}$ , [18], suggesting that it is determined primarily by the composition. This value of  $\Delta V$  can be compared to a calculation based on the Mn composition change  $\delta$  in  $(\text{La}_{0.7}\text{Sr}_{0.3})^{2.7}\text{Mn}_{1-\delta}^{3.3+\Delta V}(\text{O}_3)^{-6}$  of  $2.7 \pm 0.3\%$  measured at the same location [Fig. 1(c)], on the assumption of charge neutrality and that the valence states and composi-

tions of other elements (Sr, La, and O) are unchanged. This approach yields a Mn valence change  $\Delta V$  of  $0.09 \pm 0.01$ , in close agreement with the value derived from the  $L_3/L_2$ -edge ratio.

The change in Mn valence can be expected to be related to the spatial redistribution of charge carriers. This relationship was assessed experimentally based on the electrostatic contribution to the electron optical phase shift measured using EH, which is sensitive to local variations in electrostatic potential and mean inner potential, i.e., to charge-carrier redistribution and chemical composition change, respectively. Figure 3(b) shows the electrostatic contribution to the phase shift across the layers (black line) measured at 295 K. The profile reveals an offset between the PM and FM layers across a transition region, whose extended width is consistent with that of the charge distribution in Fig. 3(c) discussed below. It is important to note that a sharp interface region with a width of only  $\sim 7$  nm [see Fig. 1(c)] would be measured if solely the contribution from the mean inner potential were taken into account.

In order to assess the electrostatic properties of the layers, we note that the increase in average Mn valence of  $\Delta V = +0.133$  determined using EELS decreases the ideal stoichiometric 70% occupation of the Mn  $e_g$  state to 56.7% and thereby increases the free-carrier (i.e., hole) concentration in LSMO [18] from  $5 \times 10^{21} \text{cm}^{-3}$  in the FM layer to  $7.22 \times 10^{21} \text{cm}^{-3}$  in the PM layer, resulting in a step in carrier concentration at the interface. This composition-induced step in the carrier concentration is smoothed by carrier diffusion and drift, in analogy to a  $p$ - $n$  junction. The diffusion is counterbalanced by the build-up of an electric field, thereby creating a depletion-zone-like region. This situation was modeled by self-consistently solving the Poisson and continuity equations within the framework of the drift and diffusion model [23,24] for a permittivity of  $3 \times 10^4$  [25]. As shown in Fig. 3(c), the drift and diffusion of free carriers at 295 K leads to a wide transition region with a FWHM of 35 nm between the two regions with different carrier concentrations.

Furthermore, the electrostatic phase profile was simulated by considering both the charge-carrier-induced electrostatic contribution to the electrostatic potential and the Mn-concentration-difference-induced change in mean inner potential. A mean inner potential change of 0.13 V was estimated for a Mn concentration change of 3% on the basis of a mean inner potential value of 18.7 V for LSMO [26] by using a simple  $Z$ -dependent approximation for the electron scattering factors. The simulated electrostatic potential profile matches the experimental electrostatic phase shift measured using off-axis EH well, as shown in Fig. 3(b). Similarly, the calculated charge-carrier profile was used to determine the valence change profile and the expected  $\Delta L_3/L_2$ -edge ratio [Fig. 3(a), red line]. The simulated and experimental values agree well.

Both the extent of the electrostatic transition region and the penetration of FM order into the PM layer are much wider than expected for a typical magnetic proximity effect based on the exchange interaction between neighboring magnetic atoms. Because the exchange interaction is fundamentally linked to the overlap of electron wave functions and electron-electron Coulomb interactions, it is intrinsically short range. Indeed, a MuMax3 simulation [27] considering only magnetic

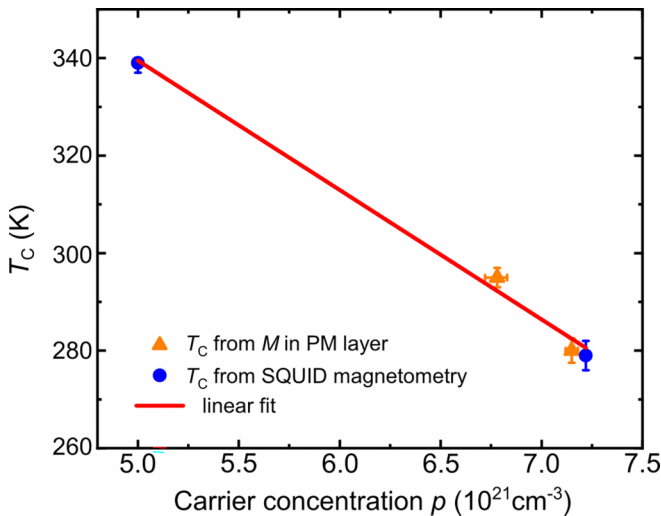


FIG. 4. Curie temperature ( $T_C$ ) determined using SQUID magnetometry (blue dots) and off-axis electron holography (orange triangles), plotted as a function of carrier concentration. The red fitting line is consistent with a linear relationship between  $T_C$  and carrier concentration.

interactions yields an interface width smaller than 1 nm and stray fields are one order of magnitude smaller and thus negligible. Interface roughness as a dominating effect can be ruled out too. Thus, in the present case, other effects, notably the free carriers, play a dominant role.

For a deeper understanding of the influence of the free-carrier density, we recall that in LSMO free holes are hopping between Mn ions along  $\text{Mn}^{3+}\text{-O}^{2-}\text{-Mn}^{4+}$  chains in the Mn  $e_g$  states. Thereby, the valence of the Mn ions varies locally and temporally, although its average value is unchanged. At the interface between PM and FM LSMO layers with different free-carrier concentrations, drift and diffusion of holes create a steady-state carrier redistribution profile, which modifies the spatial distribution of the average Mn valence and hence the  $\text{Mn}^{3+}/\text{Mn}^{4+}$  ion ratio. Since FM ordering originates from the  $\text{Mn}^{3+}\text{-Mn}^{4+}$  double exchange interaction, this change in Mn valence directly affects the density of magnetic moments, i.e., the magnetization. Simultaneously, the change in  $\text{Mn}^{3+}/\text{Mn}^{4+}$  ion ratio affects the local value of  $T_C$ .

Therefore, we determine the dependence of  $T_C$  on the free-carrier concentration as follows: First, at measurement temperatures of 295 and 280 K we find that the magnetization reaches zero at distances of  $13.3 \pm 1.8$  and  $38_{-4}^{+8}$  nm from the

chemical FM/PM interface inside the PM layer (see Fig. 2, red and blue arrows), respectively. At these distances, the measurement temperature corresponds to the local value of  $T_C$ . The corresponding values of carrier concentration can be determined from the calculation in Fig. 3(c). The resulting values of  $T_C$  vs free hole concentration are shown in Fig. 4. In addition, for the values of  $T_{C1} = 339_{-2}^{+1}$  K and  $T_{C2} = 279 \pm 3$  K of the two LSMO layers far from the interface, as determined from the SQUID measurement, the corresponding asymptotic hole concentration is given in Fig. 3(c) and included in Fig. 4. Figure 4 reveals a linear dependence of  $T_C$  on hole concentration, which can be understood in terms of a change of valence with hole concentration and thus the change in  $\text{Mn}^{3+}/\text{Mn}^{4+}$  ion ratio, which directly affects the double exchange interaction between the  $\text{Mn}^{3+}$  and  $\text{Mn}^{4+}$  ions. The importance of the determined dependence of  $T_C$  on hole concentration lies in the fact that  $T_C$  is usually affected by both strain and carrier concentration, making it impossible to obtain a clear-cut physical understanding. In the system investigated here, no strain is present and thus the carrier dependence of  $T_C$  becomes accessible. Therefore, the exceptionally long-range magnetic proximity effect that we observe is induced by the large spatial extent of the diffusion and drift of the free holes, which in turn arises from a combination of a high dielectric constant and a low free-carrier concentration when compared to a metal.

The effect that we observe here can be expected to occur widely, for example in perovskites or two-dimensional ferromagnetic materials in which the valence of the magnetic ions can be altered by a change in composition, as well as by tuning the carrier distribution through doping or application of electric fields. Our results unravel a microscopic mechanism and provide a quantitative relationship between electrostatic properties (i.e., local hole concentration and Mn valence) and local magnetization, as well as Curie temperature. This quantitative relationship defines the spatial extent of the electrostatically extended magnetic proximity effect and provides a fundamental understanding of the electrostatic shaping of nanoscale magnetism.

This project has received funding from the European Research Council (ERC) under the European Union's Horizon 2020 research and innovation program (Grant Agreement No. 856538, project "3D MAGiC"). The authors thank M. Kruth, L. Kibkalo and L. Risters for specimen preparation using focused ion beam milling as well as K. Ji, L. Jin, A. Kovács, F. Zheng, and X. Zhong for valuable discussions.

[1] F. Hellman, A. Hoffmann, Y. Tserkovnyak, G. S. D. Beach, E. E. Fullerton, C. Leighton, A. H. MacDonald, D. C. Ralph, D. A. Arena, H. A. Dürr *et al.*, *Rev. Mod. Phys.* **89**, 025006 (2017).  
 [2] L. J. Riddiford, A. J. Grutter, T. Pillsbury, M. Stanley, D. Reifsnnyder Hickey, P. Li, N. Alem, N. Samarth, and Y. Suzuki, *Phys. Rev. Lett.* **128**, 126802 (2022).  
 [3] D. Zhong, K. L. Seyler, X. Linpeng, N. P. Wilson, T. Taniguchi, K. Watanabe, M. A. McGuire, K. C. Fu, D. Xiao, W. Yao, and X. Xu, *Nat. Nanotechnol.* **15**, 187 (2020).

[4] I. Žutić, A. Matos-Abiad, B. Scharf, H. Dery, and K. Belashchenko, *Mater. Today*, **22**, 85 (2019).  
 [5] P. Wei, S. Lee, F. Lemaître, L. Pinel, D. Cutaia, W. Cha, F. Katmis, Y. Zhu, D. Heiman, J. Hone *et al.*, *Nat. Mater.* **15**, 711 (2016).  
 [6] P. K. Manna and S. M. Yusuf, *Phys. Rep.* **535**, 61 (2014).  
 [7] C. Clavero, J. R. Skuza, Y. Choi, D. Haskel, C. Sánchez-Hanke, R. Loloee, M. Zhernenkov, M. R. Fitzsimmons, and R. A. Lukaszew, *Phys. Rev. B* **80**, 024418 (2009).

- [8] J. S. Moodera, M. E. Taylor, and R. Meservey, *Phys. Rev. B* **40**, 11980 (1989).
- [9] H. B. Vasili, M. Gamino, J. Gazquez, F. Sanchez, M. Valvidares, P. Gargiani, E. Pellegrin, and J. Fontcuberta, *ACS Appl. Mater. Interfaces* **10**, 12031 (2018).
- [10] T. Moriya, *Phys. Rev.* **120**, 91 (1960).
- [11] V. K. Lazarov, M. Weinert, S. A. Chambers, and M. Gajdardziska-Josifovska, *Phys. Rev. B* **72**, 195401 (2005).
- [12] C. Kim and Y.-C. Chung, *Appl. Phys. Lett.* **88**, 132512 (2006).
- [13] S. V. Eremeev, V. N. Men'shov, V. V. Tugushev, P. M. Echenique, and E. V. Chulkov, *Phys. Rev. B* **88**, 144430 (2013).
- [14] X. Qian and W. Hübner, *Phys. Rev. B* **67**, 184414 (2003).
- [15] R. Tyer, G. van der Laan, W. M. Temmerman, Z. Szotek, and H. Ebert, *Phys. Rev. B* **67**, 104409 (2003).
- [16] E.-M. Choi, K. I. Sim, K. S. Burch, and Y. H. Lee, *Adv. Sci.* **9**, 2200186 (2022).
- [17] See Supplemental Material at <http://link.aps.org/supplemental/10.1103/PhysRevB.108.L180410> for sample preparation, temperature measurement, TEM characterization, and determination of out-of-plane magnetization by electron holographic tomography.
- [18] Q. Lan, C. Wang, L. Jin, M. Schnedler, L. Freter, K. Fischer, J. Caron, X.-K. Wei, T. Denneulin, A. Kovács *et al.*, *Phys. Rev. Lett.* **129**, 057201 (2022).
- [19] M. W. Haverkort, S. I. Csiszar, Z. Hu, S. Altieri, A. Tanaka, H. H. Hsieh, H. J. Lin, C. T. Chen, T. Hibma, and L. H. Tjeng, *Phys. Rev. B* **69**, 020408 (2004).
- [20] J. Caron, Ph.D. thesis, RWTH Aachen University, 2017.
- [21] T. Kasama, M. Beleggia, and R. E. Dunin-Borkowski, *Electron Holography of Magnetic Materials* (IntechOpen London, United Kingdom, 2011), pp. 57–61.
- [22] M. Varela, M. P. Oxley, W. Luo, J. Tao, M. Watanabe, A. R. Lupini, S. T. Pantelides, and S. J. Pennycook, *Phys. Rev. B* **79**, 085117 (2009).
- [23] M. Schnedler, R. E. Dunin-Borkowski, and P. Ebert, *Phys. Rev. B* **93**, 195444 (2016).
- [24] M. Schnedler, V. Portz, P. H. Weidlich, R. E. Dunin-Borkowski, and P. Ebert, *Phys. Rev. B* **91**, 235305 (2015).
- [25] S. Majumdar, H. Huhtinen, P. Paturi, and H. S. Majumdar, *J. Mater. Sci.* **48**, 2115 (2013).
- [26] T. Kasama, M. S. Moreno, R. E. Dunin-Borkowski, S. B. Newcomb, N. Haberkorn, J. Guimpel, and P. A. Midgley, *Appl. Surf. Sci.* **252**, 3977 (2006).
- [27] A. Vansteenkiste, J. Leliaert, M. Dvornik, M. Helsen, F. Garcia-Sanchez, and B. Van Waeyenberge, *AIP Adv.* **4**, 107133 (2014).